

# Manipulating Nanoparticle Aggregates Regulates Receptor–Ligand Binding in Macrophages

Yuri Kim,<sup>¶</sup> Hee Joon Jung,<sup>¶</sup> Yunjung Lee, Sagang Koo, Ramar Thangam, Woo Young Jang, Seong Yeol Kim, Sangwoo Park, Sungkyu Lee, Gunhyu Bae, Kapil Dev Patel, Qiang Wei, Ki-Bum Lee, Ramasamy Paulmurugan, Woong Kyo Jeong, Taeghwan Hyeon, Dokyoon Kim,<sup>\*</sup> and Heemin Kang<sup>\*</sup>



Cite This: <https://doi.org/10.1021/jacs.1c08861>



Read Online

ACCESS |



Metrics & More

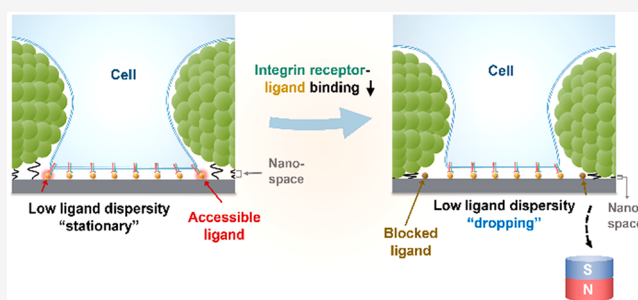


Article Recommendations



Supporting Information

**ABSTRACT:** The receptor–ligand interactions in cells are dynamically regulated by modulation of the ligand accessibility. In this study, we utilize size-tunable magnetic nanoparticle aggregates ordered at both nanometer and atomic scales. We flexibly anchor magnetic nanoparticle aggregates of tunable sizes over the cell-adhesive RGD ligand (Arg-Gly-Asp)-active material surface while maintaining the density of dispersed ligands accessible to macrophages at constant. Lowering the accessible ligand dispersity by increasing the aggregate size at constant accessible ligand density facilitates the binding of integrin receptors to the accessible ligands, which promotes the adhesion of macrophages. In high ligand dispersity, distant magnetic manipulation to lift the aggregates (which increases ligand accessibility) stimulates the binding of integrin receptors to the accessible ligands available under the aggregates to augment macrophage adhesion-mediated pro-healing polarization both *in vitro* and *in vivo*. In low ligand dispersity, distant control to drop the aggregates (which decreases ligand accessibility) repels integrin receptors away from the aggregates, thereby suppressing integrin receptor–ligand binding and macrophage adhesion, which promotes inflammatory polarization. Here, we present “accessible ligand dispersity” as a novel fundamental parameter that regulates receptor–ligand binding, which can be reversibly manipulated by increasing and decreasing the ligand accessibility. Limitless tuning of nanoparticle aggregate dimensions and morphology can offer further insight into the regulation of receptor–ligand binding in host cells.



## INTRODUCTION

In the natural microenvironment, dynamic binding of cell receptors to the ligands is modulated by the regulation of ligand accessibility, which triggers biochemical reactions. The modulation of accessible ligands plays a pivotal role in dynamic regulation of the development and function of tissues.<sup>1–3</sup> Developing materials<sup>4</sup> with tunability of accessible ligand dispersity can regulate and unravel dynamic receptor–ligand interactions<sup>5,6</sup> and subsequent immune cell responses,<sup>7–14</sup> such as macrophage adhesion and polarization.<sup>15,16</sup> Meanwhile, spatial organization of RGD ligand-bearing nanoparticles<sup>17–20</sup> has been demonstrated in various ways by modulating the presentation of entirely exposed ligands (without modulating ligand accessibility), such as ligand ordering,<sup>21</sup> ligand micro-patterning,<sup>22</sup> ligand localization,<sup>23,24</sup> ligand interspacing (density),<sup>25,26</sup> ligand clustering,<sup>27</sup> and dynamic ligand stretching.<sup>28</sup> Multimodal manipulation of the accessible ligand dispersity on materials could effectively regulate the binding of integrin receptors to the accessible ligands<sup>29</sup> in macrophages that modulate host responses.<sup>30–32</sup>

It has been shown that cellular adhesion (the result of integrin receptors binding to the accessible ligands) can be

regulated by harnessing various types of materials<sup>33–35</sup> that exhibit responsiveness to pH change,<sup>36</sup> ultrasound, and various spectra of light stimuli,<sup>37–42</sup> such as ultraviolet (UV)<sup>43</sup> and near-infrared light.<sup>44</sup> In particular, materials that can irreversibly expose the ligands via light stimulation have been reported,<sup>43,45</sup> in which the UV-light-mediated irreversible ligand unblocking strategy was used to modulate host macrophage adhesion. However, the use of such materials is limited due to their irreversibility and usage of harmful UV light that is readily absorbed by living tissues.<sup>43</sup> In studies with more sophisticated control, materials that allow distant manipulation of ligand unblocking and blocking via light stimulation were reported using photoswitchable azobenzene derivatives and self-assembled monolayers, but were limited to *in vitro* experiments only.<sup>46–48</sup> On the other hand, a magnetic

Received: August 22, 2021



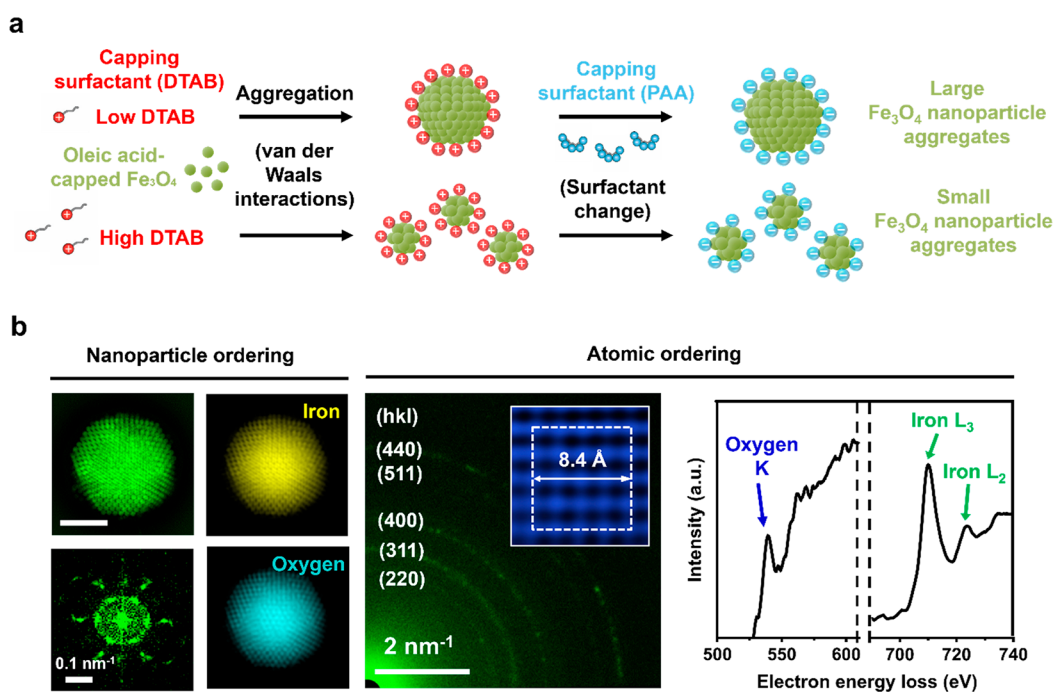


**Figure 1.** Synthesis of magnetic nanoparticle aggregates via capping surfactant-mediated size tuning ordered at nanometer and atomic scales. (a) Chemical reaction strategies of capping surfactant (DTAB)-regulated aggregate size tuning of  $\text{Fe}_3\text{O}_4$  nanoparticle ensemble closed-packed at nanometer and atomic scales. (b) A high angle annular dark field-scanning transmission electron microscopy (HAADF-STEM) image, a fast Fourier transform (FFT) analysis, and the elemental composition of iron and oxygen of the  $\text{Fe}_3\text{O}_4$  nanoparticle aggregates exhibiting nanoscale ordering. The scale bars represent 100 nm for the HAADF-STEM image and elemental maps, and  $0.1 \text{ nm}^{-1}$  for the FFT analysis. Selected area diffraction (SAD) pattern of 200 nm  $\text{Fe}_3\text{O}_4$  nanoparticle aggregates exhibiting atomic ordering. The concentric rings have been indexed to the (hkl) diffraction planes of the  $\text{Fe}_3\text{O}_4$  phase in the nanoparticles randomly oriented in the aggregates. The scale bars represent  $2 \text{ nm}^{-1}$ . Inset shows HAADF-STEM image of the atomic arrangement in the crystalline  $\text{Fe}_3\text{O}_4$  nanoparticles. The lattice parameter of the inverse spinel structure in the  $\text{Fe}_3\text{O}_4$  phase is labeled. Electron energy loss spectroscopy (EELS) spectra of iron and oxygen in the 200 nm  $\text{Fe}_3\text{O}_4$  nanoparticle aggregates with the peaks labeled for iron  $L_3$  (710 eV) and  $L_2$  (723 eV), and oxygen K (539 eV).

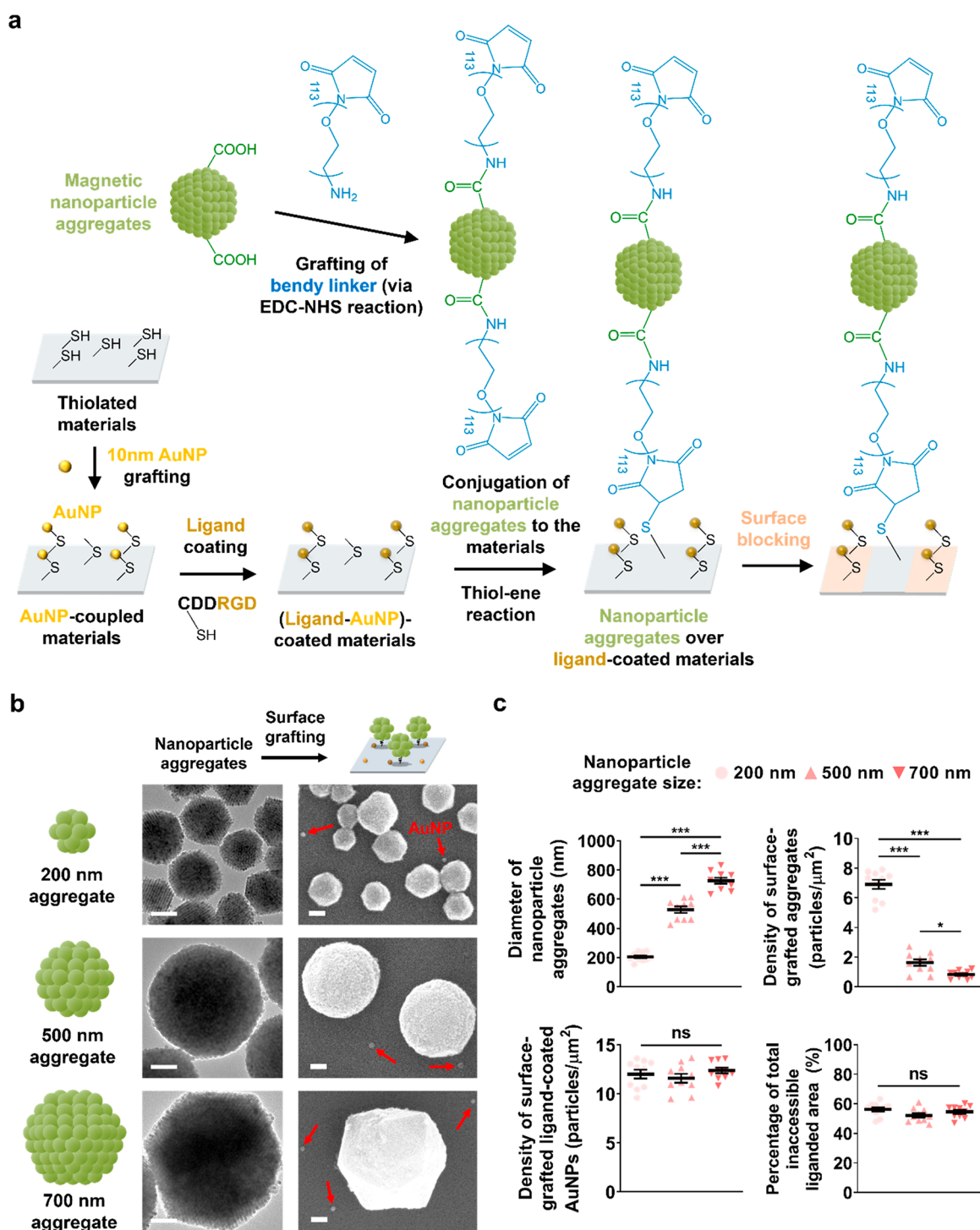
field<sup>49–54</sup> is another stimulus that can actively manipulate dynamic ligand presentation on materials. Our group has recently revealed the magnetic control of ligand nano-uncoiling,<sup>55</sup> ligand nanobarcoding,<sup>56</sup> planar ligand motion,<sup>57</sup> ligand-bearing nanoparticle uncaging,<sup>58</sup> and others. For instance, magnetic nanoparticles and ligand-bearing nanoparticles in heterodimeric structures switched their conformational states to “entirely” expose or hide the ligands, thereby regulating the ligand accessibility of integrins.<sup>58</sup> However, this prior approach is limited due to the lack of “multimodal” adjustability of ligand exposure on the entire material surface. The design of materials that can modulate the ligand accessibility via magnetic field could be realized via synthesis of magnetic nanoparticle aggregates in defined sizes by strictly controlling the aggregation<sup>59</sup> of magnetic nanoparticles.

In this study, we employed materials to demonstrate multimodal and reversible manipulation of the ligand accessibility on material surfaces to regulate receptor–ligand binding. We synthesized magnetic nanoparticle aggregates by controlling the aggregation of magnetic nanoparticles ordered at both nanometer and atomic scales with capping surfactant-mediated tuning of the aggregate sizes (200, 500, and 700 nm). These aggregates in various sizes were anchored to a thiolated material surface pre-decorated with liganded gold nanoparticles (AuNPs) via bendy linkers. The accessible ligand dispersity on this material was altered depending on the aggregate size, while the accessible ligand density remained the same regardless of the aggregate size. In the “stationary” condition (without applying a magnet), binding of integrin receptors to the

accessible ligands was shown to be augmented proportionally with the elevation of aggregate size, which lowers the accessible ligand dispersity. These findings suggest that the low dispersity of partially accessible ligands facilitates cellular adhesion, which is apparently different from previous studies in which cellular regulation was achieved via modulating “entirely” exposed ligand clustering<sup>27</sup> and localization.<sup>23</sup> By applying an external magnetic field, lifting (i.e., increasing the ligand accessibility) or dropping (i.e., decreasing the ligand accessibility) the aggregates via linker straightening and bending, respectively, were distantly manipulated both *in vitro* and *in vivo*. This manipulation advances from prior *in vivo* demonstrations that utilized heterodimers for the “entire” unblocking or blocking of the accessible ligands on material surface (without the capability of partial unblocking)<sup>58</sup> or those that utilized UV-light-mediated “entire” ligand unblocking (without the capability of partial unblocking and reversibility).<sup>43</sup>

## RESULTS AND DISCUSSION

**Synthesis of Magnetic Nanoparticle Aggregates with Capping Surfactant-Mediated Size Tuning.** Distant manipulation of multimodal ligand dispersity was enabled by synthesizing magnetic nanoparticle aggregates of adjustable sizes (200, 500, and 700 nm in diameters), which effectively modulates the accessibility of the significantly smaller 10 nm-sized ligand-coated AuNPs (Figure 1a). First, we synthesized  $\text{Fe}_3\text{O}_4$  nanoparticles using iron-oleate complex,<sup>60</sup> to which cationic surfactant [dodecyltrimethylammonium bromide (DTAB)] was added. The suspension containing DTAB



surrounded  $\text{Fe}_3\text{O}_4$  nanoparticles in micelles, and was subjected to solvent evaporation to facilitate the aggregation of oleic acid-capped  $\text{Fe}_3\text{O}_4$  nanoparticles into spherical morphology via van der Waals interactions. By modulating the amount of

surfactants that cap the magnetic nanoparticle aggregates (the ensemble of  $\text{Fe}_3\text{O}_4$  nanoparticles), the size of the aggregates was precisely regulated. Increasing the amount of capping surfactants resulted in increased capping of total aggregate

surface area, thereby yielding smaller-sized aggregates in higher quantity. Later, DTAB was replaced with polyanions [poly(acrylic acid), PAA] via direct surface binding of PAA due to the high affinity of the carboxylate group in PAA to the surface of  $\text{Fe}_3\text{O}_4$  aggregates.

The  $\text{Fe}_3\text{O}_4$  nanoparticle aggregates ordered at nanometer scale were confirmed by high angle annular dark field-scanning transmission electron microscopy (HAADF-STEM) imaging (Figure 1b). Fast Fourier transform (FFT) analysis exhibited hexagonal array spots, thereby revealing the close packing of aggregated  $\text{Fe}_3\text{O}_4$  nanoparticles (Figure 1b). Selected area diffraction (SAD) analysis of the nanoparticle aggregates showed multiple concentric diffraction rings, thereby indicating the random orientation of the  $\text{Fe}_3\text{O}_4$  nanoparticles (Figure 1b and Supplementary Figure S1a). Through the analysis of interplanar  $d$ -spacings, diffraction rings were found to correspond to the (220), (311), (400), (422), (511), and (440) planes of the  $\text{Fe}_3\text{O}_4$  nanoparticles. High resolution-STEM (HR-STEM) images divulged that the atomic arrangement within the crystalline  $\text{Fe}_3\text{O}_4$  nanoparticles in aggregates correspond to the inverse spinel structure of the  $\text{Fe}_3\text{O}_4$  phase (Figure 1b). The elemental composition of iron and oxygen in the  $\text{Fe}_3\text{O}_4$  nanoparticle aggregates was evident in both the elemental maps and the electron energy loss spectroscopy (EELS) analysis consistently with the previously analyzed data,<sup>61</sup> thereby confirming that the elemental composition of  $\text{Fe}_3\text{O}_4$  nanoparticles was retained and their magnetic property was maintained after aggregation (Figure 1b).

Zeta potential measurements verified that the polyanion-capped nanoparticle aggregates of adjustable size were negatively charged (Supplementary Figure S1b). Peaks at 2919 and 2852  $\text{cm}^{-1}$  in Fourier transform infrared (FTIR) spectra of iron oxide nanoparticles demonstrate the formation of oleic acid capped- $\text{Fe}_3\text{O}_4$  nanoparticles (Supplementary Figure S2). After adding anionic surfactants to cationic surfactant-capped nanoparticle aggregates to obtain the final product, peaks at 1570 and 1416  $\text{cm}^{-1}$  are formed, which are the characteristic peaks of the  $\text{COO}^-$ -Fe bond. Moreover, the absence of cationic surfactant (DTAB) peaks, such as  $\text{N}(\text{CH}_3)_3$  at 1481  $\text{cm}^{-1}$ , confirm the replacement of DTAB with PAA. Low magnification transmission electron microscopy (TEM) images and dynamic light scattering (DLS) analysis collectively validated the nearly monodisperse size distribution of each nanoparticle aggregate group (200, 500, and 700 nm) with spherical and slightly polyhedral morphology (Supplementary Figure S3a,b). Analyses of each group for their diameters were computed as  $209.6 \pm 5.1$  nm (200 nm group),  $496.2 \pm 7.4$  nm (500 nm group), and  $708.5 \pm 18.8$  nm (700 nm group), respectively. Vibrating sample magnetometry (VSM) measurements showed negligible coercivity in the hysteresis loops of the nanoparticle aggregates of adjustable size, thereby verifying their reversible magnetization property (Supplementary Figure S3c).

**Modulation of the Accessible Ligand Dispersity.** The magnetic nanoparticle aggregates of adjustable size were situated over the ligand-active material surface to present various levels of accessible ligand dispersity while maintaining constant accessible ligand density. To prepare the material presenting ligand-bearing AuNPs, 10 nm AuNPs which exhibited atomic-level crystallinity were synthesized, as shown in the high resolution-STEM image (Supplementary Figure S4a). First, the AuNPs were anchored onto the thiol group-presenting material surface. Then, the thiol group in the

cysteine-bearing RGD tripeptide<sup>62</sup> ligands was grafted to the AuNPs that were pre-grafted on the material surface. In this study, we have chosen RGD ligands to observe the maximized effect of macrophage adhesion regulation since macrophage adhesion is facilitated the most in the presence of RGD among other cell-adhesive ligands that exist in the ECM.<sup>63</sup> The analysis of the density of RGDs grafted to the AuNPs on the material surface using thiol detection assay revealed that  $406.0 \pm 50.1$  RGDs were grafted per AuNP. The scanning electron microscopy (SEM) images demonstrated the homogeneous distribution of ligand-coated AuNPs grafted to the material surface with AuNP density of  $12.0 \pm 1.4$  nanoparticles/ $\mu\text{m}^2$  (Supplementary Figure S4b). A bendy linker, maleimide-poly(ethylene glycol) (PEG)-amine ( $M_w$ : 5 kDa) was used to coat the surface of the PAA-capped magnetic aggregates via EDC/NHS coupling between the amine groups in the linker and the carboxylate groups in the PAA-capped aggregates (Figure 2a). The polymer linker-conjugated aggregates were grafted to the thiolated material surface presenting ligand-coated AuNPs via thiol-ene reaction between the maleimide and thiol group on the material surface. This was possible since the length of the polymer linker used in this study has been reported to be roughly 38 nm, which is substantially longer than the 10 nm sized AuNPs.<sup>64,65</sup> As a result, magnetic nanoparticle aggregates of adjustable size were uniformly anchored to the ligand-active material surface, which created spaces between the lower side of the spherical aggregates and the underlying liganded AuNPs (Figure 2b). The 10 nm AuNPs were used in this study due to their size being comparable to that of the integrin receptor to enable the recruitment of a single integrin receptor molecule to each liganded AuNP.<sup>66</sup>

By lowering the concentration of the aggregates with increasing aggregate size, the surface-grafted density of the aggregates was gradually decreased, while maintaining a similar total area of accessible ligands on the material surface; the densities of the surface-grafted aggregates were computed as  $6.7 \pm 0.3$ ,  $1.6 \pm 0.1$ , and  $0.8 \pm 0.1$  aggregates/ $\mu\text{m}^2$  for 200, 500, and 700 nm aggregates, respectively (Figure 2c). The percentages of total inaccessible liganded area of adjustable size were comparable (ranging from 52.0% to 56.2%), thereby maintaining similar total area of accessible ligands with various degrees of accessible ligand dispersity. We believe that this percentage of inaccessible area was sufficiently high to effectively regulate the integrin receptor-ligand binding by lifting or dropping the magnetic aggregates, which increased or decreased the ligand accessibility, respectively.

**Modulating the Accessible Ligand Dispersity Solely Alters Macrophage Adhesion.** The thiolated material surface free of anchored magnetic nanoparticle aggregates and ligand-coated AuNPs was blocked by methoxy-PEG-maleimide via the thiol-ene reaction to ensure the accessible ligand dispersity-specific macrophage regulation. The independent effect of modulating accessible ligand dispersity using magnetic aggregates of adjustable size (“high”, “moderate”, and “low” ligand dispersity with the 200, 500, and 700 nm aggregates, respectively) with constant total area of accessible ligands on the assembly of macrophage adhesion complexes was explored without a magnet (“stationary” condition) after culturing them for 24 h on the materials covered with magnetic nanoparticle aggregates over the ligand-coated AuNPs. The macrophages were only plated onto the materials only at the initial stage, which was considered 0 h. Pronounced

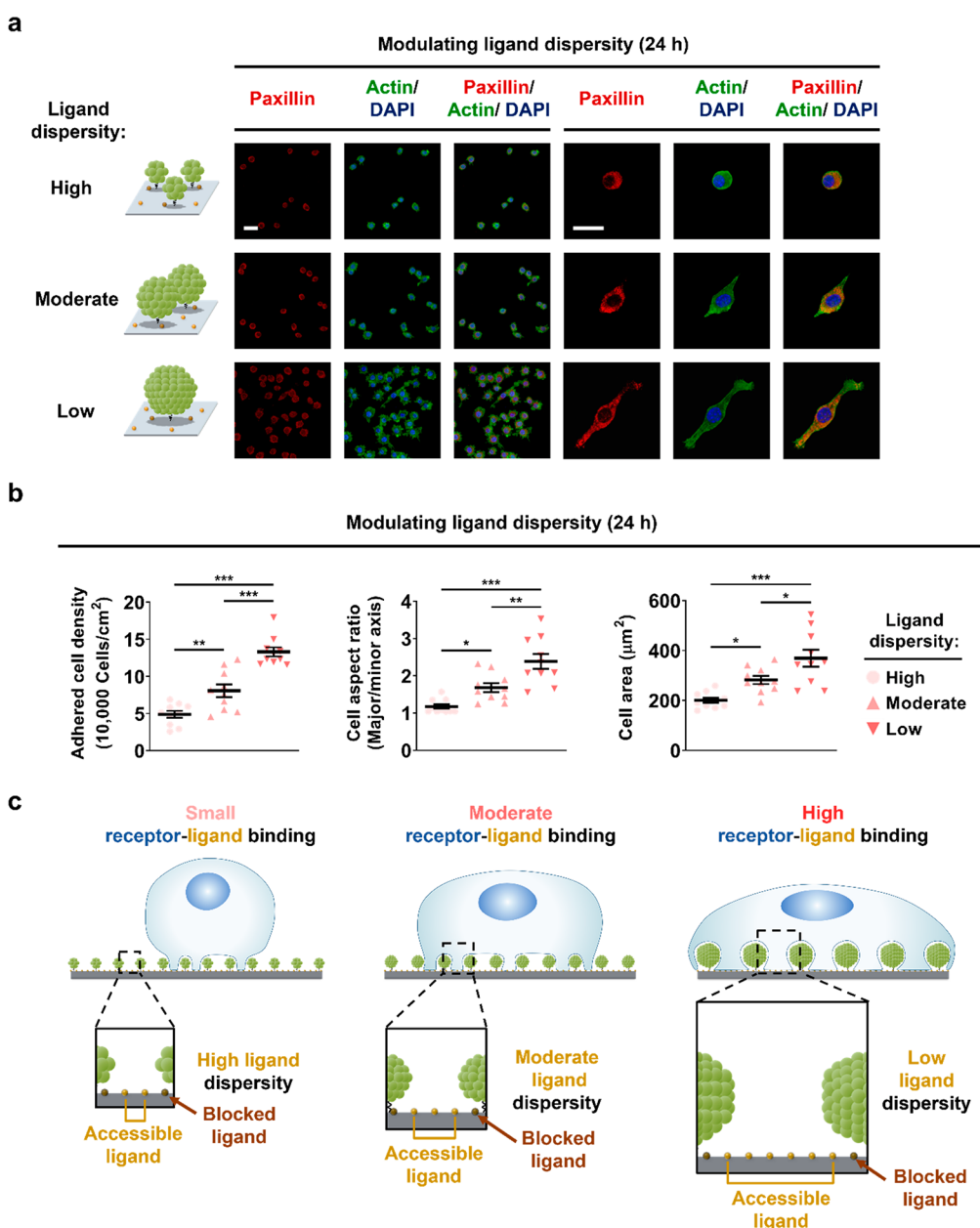


**Figure 3.** Lowering ligand dispersity stimulates receptor–ligand binding in macrophage adhesion independent of the ligand density. (a) Immunofluorescently stained images of F-actin, paxillin, and DAPI (nuclei) of adherent macrophages after 24 h of culturing in the presence of high, moderate, and low accessible ligand dispersity at low and high magnifications. The scale bars indicate 20  $\mu\text{m}$ . (b) Calculations of the adherent macrophage density, aspect ratio, and spread area from each of the acquired images in (a). (c) The proposed model demonstrating the independent effect of increasing the size of magnetic nanoparticle aggregates (i.e., lowering the ligand dispersity) on augmenting the recruitment of integrin receptors to the accessible ligands. Data are shown as the mean  $\pm$  standard error ( $n = 10$ ). Asterisks were assigned to  $p$  values with statistically significant differences ( $*p < 0.05$ ;  $**p < 0.01$ ;  $***p < 0.001$ ).

expressions of cytoskeletal proteins (F-actin and paxillin) were observed for “low” dispersity, which was gradually reduced from “moderate” to “high” dispersity, as observed in the immunofluorescently stained images (Figure 3a). Corresponding computations show significantly higher adhesion density, aspect ratio (i.e., an elongated shape), and spread area in adherent macrophages as the ligand dispersity is gradually lowered (Figure 3b). These findings suggest that the assembly of macrophage adhesion complexes was proportionally augmented with lowered ligand dispersity despite constant accessible ligand density. We propose that two factors affect macrophage adhesion in our system: ligand dispersity and

membrane bending. Since nanostructured materials with high curvature can reduce the energy barrier of membrane bending, cellular membrane bending on our aggregate-conjugated material surface will remain stable compared to other pillar-structured materials.<sup>67,68</sup> It has been known that if the interspacing of nanostructures becomes smaller, cells do not engulf the nanostructure and are likely to stay on the top of the nanostructure.<sup>69–71</sup> Therefore, the cells are not likely to entirely reach the RGD ligand-coated surface on higher ligand dispersity groups since the density of aggregates becomes higher with higher ligand dispersity. Furthermore, in the lower ligand dispersity group, ligand clustering is favorable due to

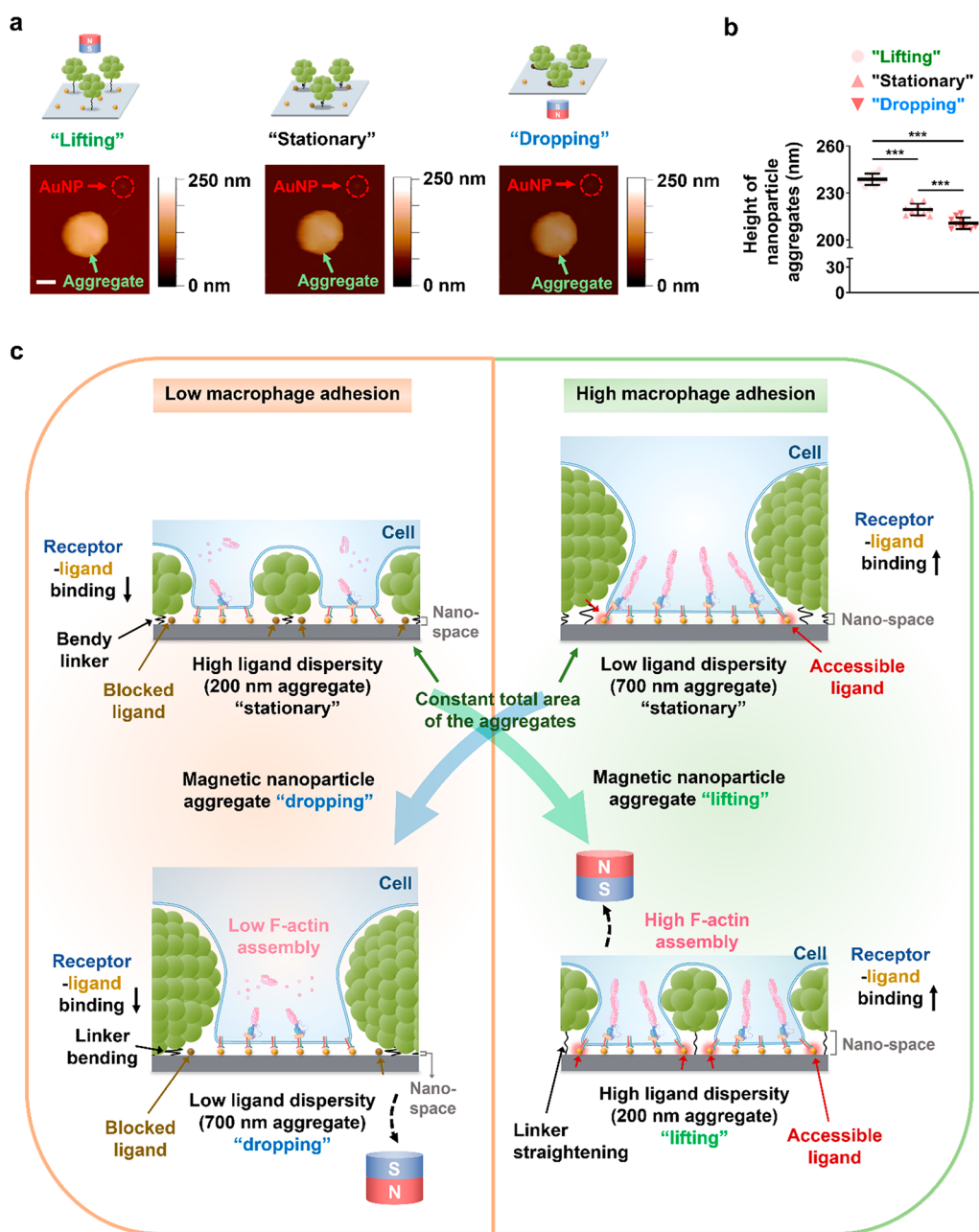


**Figure 4.** Distant manipulation of lifting or dropping the magnetic nanoparticle aggregates relatively increases or decreases the ligand accessibility, respectively. (a) In situ magnetic atomic force microscopy (AFM) images of the distant magnetic manipulation for “lifting” or “dropping” the 200 nm nanoparticle aggregates (indicated by green arrows), thereby increasing and decreasing the liganded AuNP accessibility [appearing faint due to small size (10 nm), indicated by red arrows], and “stationary” nanoparticle aggregates (without applying a magnet). The scale bar indicates 100 nm. (b) Computations of the heights of the 200 nm magnetic nanoparticle aggregates in “lifting”, “stationary”, and “dropping” conditions. (c) A schematic demonstrating the distant magnetic attraction of the 200 nm magnetic nanoparticle aggregates (high accessible ligand dispersity) for “lifting” them via straightening of the polymer linker, which augments the integrin receptor–ligand binding in macrophages that are repressed in the “stationary” (nonmagnetized) condition. Remotely controlled “dropping” of the 700 nm magnetic nanoparticle aggregates (low accessible ligand dispersity) via bending of the polymer linker deactivates the integrin receptor–ligand binding in macrophages that is activated in the “stationary” condition. Data are displayed as the mean  $\pm$  standard error ( $n = 10$ ). Asterisks were assigned to  $p$  values with statistically significant differences ( $***p < 0.001$ ).

accessible ligand dispersity. To summarize, when the ligand dispersity is lower, it is more likely for the cells to reach the RGD-coated surface after engulfment, thereby stimulating the integrin receptor–ligand binding and cell spreading (Figure 3c).

Negative control experiments conducted on material surfaces with non-ligand-coated AuNPs (without aggregates) and material surfaces with magnetic aggregates grafted over

non-ligand-coated AuNPs exhibited minimal macrophage adhesion over all ligand dispersity groups without significant differences as evidenced by the immunofluorescently stained images and corresponding quantifications (Supplementary Figure S5a,b). Additionally, other negative control experiments conducted on bare substrates and substrates with only magnetic aggregates (without AuNPs) demonstrated the inhibition of macrophage adhesion in all ligand dispersity

groups without significant differences (Supplementary Figure S6a,b). These results prove that the ligand dispersity modulation-specific macrophage regulation is accomplished with the assistance of RGD ligands on AuNPs, which is essential to facilitate macrophage adhesion via integrin receptor binding to cell-adhesive RGD ligands. These results are apparently different from those in previous reports that modulate the “entirely” accessible ligand clustering<sup>27</sup> and localization<sup>23</sup> for cell regulation, which showed how cells respond to the clustered RGDs via exploring the effect of fully accessible ligands without partial manipulation of the ligand accessibility. On the other hand, we have regulated the ligand dispersity by partially modulating the ligand accessibility, which can be further tuned by magnetic field-based control.

**Independent Modulation of the Accessible Ligand Dispersity via Distant Manipulation.** Lifting of the magnetic aggregates via polymer linker straightening expands the nanospaces between the aggregates and the underlying ligands, thereby increasing the ligand accessibility. Dropping the magnetic aggregates via bending of the polymer linker reduces the nanospaces between the aggregates and the underlying ligands, thereby relatively decreasing the ligand accessibility. This distant manipulation of the magnetic aggregate movement was validated via in situ magnetic atomic force microscopy (AFM). The measurement of the strength of a permanent magnet (as a function of distance from the magnet) used for AFM analysis and all of the in vitro experiments verified that approximately 290 mT magnetic field was applied to the magnetic aggregates (Supplementary Figure S7). An identical area of the material surface presenting magnetic aggregates over liganded AuNPs was imaged three times either with (“lifting” or “dropping” aggregate condition) or without a permanent magnet (“stationary” aggregate condition). Three images of “lifting”, “stationary”, and “dropping” conditions exhibited markedly different contrasts of the magnetic aggregates, thereby indicating significantly different heights of the magnetic aggregates ( $237.7 \pm 0.6$  nm,  $218.3 \pm 1.5$  nm, and  $209.7 \pm 2.5$  nm, respectively) (Figure 4a,b). The 10 nm AuNPs appeared faint due to their low height. The difference in the heights of the magnetic aggregates (28.0 nm) during distant manipulation significantly modulated the spaces between the magnetic aggregates and the underlying ligands, which effectively regulated the recruitment of integrin receptors (10 nm) in cells. The lateral dimension and spherical morphology of the magnetic aggregates remained unchanged during distant manipulation. Comparable height changes of the magnetic aggregates with adjustable sizes (500 and 700 nm) under distant manipulation by bending and straightening of the identical length bendy polymer linker were also verified. The height of the 500 nm magnetic aggregate in “lifting”, “stationary”, and “dropping” conditions was measured to be  $549.6 \pm 0.8$  nm,  $528.6 \pm 0.5$  nm, and  $521.6 \pm 0.9$  nm, respectively (Supplementary Figure S8a). The height of the 700 nm  $\text{Fe}_3\text{O}_4$  aggregate was measured as  $757.8 \pm 0.5$  nm,  $737.5 \pm 0.4$  nm, and  $722.0 \pm 0.5$  nm in “lifting”, “stationary”, and “dropping” conditions, respectively (Supplementary Figure S8b). The maximum height differences were calculated to be 28.0, 28.1, and 35.7 nm for 200, 500, and 700 nm  $\text{Fe}_3\text{O}_4$  aggregates, respectively, which verified that the degree of the height modulation is consistent in all of the groups with different magnetic aggregate sizes. To mimic in vivo conditions, we placed the same permanent magnet far from the  $\text{Fe}_3\text{O}_4$  aggregates (yielding 200 mT) in approximately 10

mm distance from the materials and conducted AFM analysis under this distant manipulation (Supplementary Figures S9–S10). The heights of 200 nm nanoparticle aggregates were  $239.7 \pm 0.6$  nm,  $219.9 \pm 0.7$  nm, and  $211.0 \pm 0.3$  nm for “lifting”, “stationary”, and “dropping” conditions, respectively. For 700 nm nanoparticle aggregates, the heights were  $752.2 \pm 0.2$  nm,  $737.9 \pm 0.5$  nm, and  $722.4 \pm 0.5$  nm for “lifting”, “stationary”, and “dropping” conditions, respectively. These findings suggest that the height difference is saturated under distant manipulation for both in vitro and in vivo conditions.

**Distant Manipulation of Ligand Accessibility Modulation Controls Receptor–Ligand Binding in Macrophages.** The effect of distant manipulation of the dynamic variation in the accessible ligand dispersity on integrin receptor binding to the accessible ligands in macrophages was investigated after 24 h of culturing (Figure 4c). The permanent magnet was situated nearby the cultures to direct the “lifting” or “dropping” of the magnetic aggregates, thereby relatively increasing or decreasing the accessibility of integrin receptors to the underlying ligands, respectively, whereas the “stationary” condition without the magnet was used as a control. Two distinct groups (“high” and “low” accessible ligand dispersity, which exhibit low and high levels of macrophage adhesion, respectively) in the “stationary” condition were subjected to this distant manipulation. In the “high” ligand dispersity, the “lifting” of the magnetic aggregates, which relatively increased the nanospace between bottom hemisphere of aggregates and underlying RGD ligand-coated surface, promotes the binding of integrin receptors to the ligands and significantly augmented macrophage adhesion. Since the nanospace in the “stationary” state of the “high” ligand dispersity is already too small for the cell to reach underneath the aggregates, the “dropping” of the magnetic aggregates, which decreased the ligand accessibility, did not significantly inhibit macrophage adhesion compared to the “stationary” group. Therefore, “stationary” and “dropping” groups in “high” ligand dispersity both inhibited macrophage adhesion compared to “lifting” group as analyzed from the immunofluorescently stained images and corresponding quantifications (Supplementary Figure S11a,b). To summarize, only the “lifting” direction was effective for “high” ligand dispersity to significantly modulate macrophage adhesion via distant manipulation. In contrast, in the “low” ligand dispersity, the “dropping” of the magnetic aggregates, which decreased nanospace and the ligand accessibility, significantly suppressed macrophage adhesion compared to the “stationary” group (Supplementary Figure S11c,d). As a nanospace in the “stationary” state of the “low” ligand dispersity is sufficiently high for the cells to bend and enter underneath the aggregates, the “lifting” group negligibly augmented macrophage adhesion compared to the “stationary” group. Thus, only the “dropping” direction was effective for the “low” ligand dispersity to effectively control the macrophage adhesion via distant manipulation. Therefore, the distant manipulation has selective directional effectivity depending on the size of aggregates, which is illustrated in Supplementary Figure S12.

The effective “lifting” of the “high” ligand dispersity to significantly augment macrophage adhesion and the “dropping” of the “low” ligand dispersity to significantly suppress macrophage adhesion are summarized in Figure 4c. Moreover, these two phenomena were employed for further detailed investigations. The effect of distant manipulation of increasing or decreasing the ligand accessibility to vary the ligand dispersity on the expression and recruitment of integrin

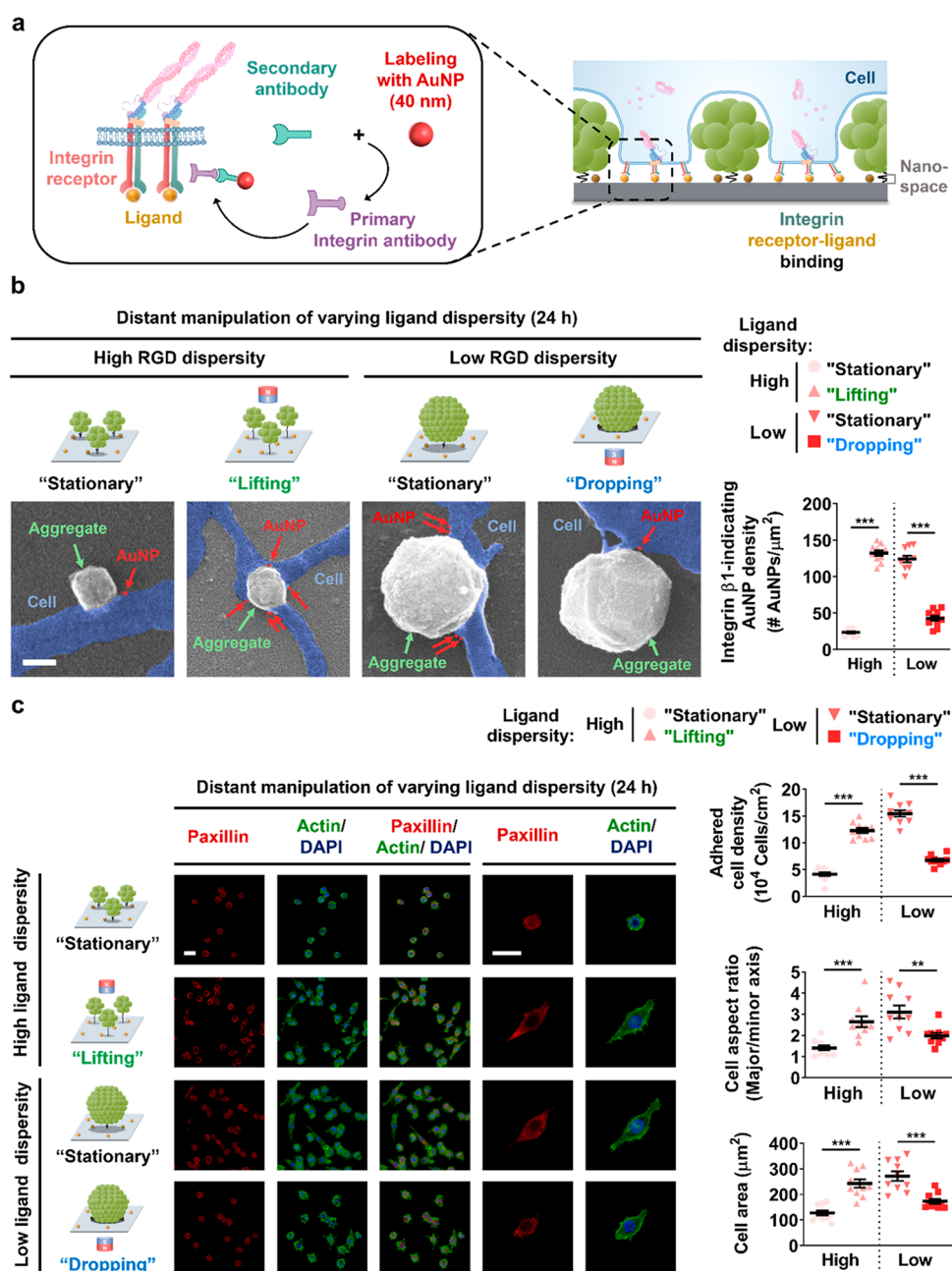


**Figure 5.** Integrin receptors actively bind to the accessible ligands to augment macrophage adhesion under the low ligand dispersity or by lifting the magnetic nanoparticle aggregates via distant manipulation. (a) A schematic of the AuNP-based immunolabeling of integrin  $\beta 1$  in macrophages and (b) scanning electron microscopy (SEM) images of adherent macrophages (blue color) highlighting the recruitment of integrin  $\beta 1$  to the accessible ligand immunolabeled with AuNPs (red color) and calculation of the integrin  $\beta 1$  density (indicating the attached AuNPs) in each cell after 24 h of culturing with high accessible ligand dispersity (the "stationary" and "lifting" groups) and low accessible ligand dispersity (the "stationary" and "dropping" groups). The magnetic nanoparticle aggregates are indicated by green arrows. The scale bar indicates 200 nm. (c) Immunofluorescently stained images of F-actin, paxillin, and DAPI (nuclei) of adherent macrophages after 24 h of culturing in high accessible ligand dispersity (the "stationary" and "lifting" groups) as well as low accessible ligand dispersity (the "stationary" and "dropping" groups) at low and high magnifications. The scale bars indicate 20  $\mu\text{m}$ . Calculations of the adherent macrophage density, aspect ratio, and spread area from each of the acquired images in (c) were statistically compared separately in each high or low accessible ligand dispersity group using a two-tailed Student's *t* test. Asterisks were assigned to *p* values with statistically significant significances (\*\**p* < 0.01; \*\*\**p* < 0.001). Data are presented as the mean  $\pm$  standard error (*n* = 10).

receptors in macrophages was investigated by immunofluorescent staining and by nanoscale immunogold labeling, respectively (Figure 5a,b and Supplementary Figure S13a,b). Recruited integrin  $\beta 1$  in the adherent macrophages after 24 h of culturing was immunolabeled with 40 nm AuNPs such that they could be differentiated from the liganded 10 nm-sized

AuNPs on the material surface (Figure 5a). The expression and recruitment of integrin  $\beta 1$  were found to have been significantly stimulated in the "lifting" group (moving the magnetic aggregates upward) compared to the "stationary" group of "high" ligand dispersity (Figure 5b and Supplementary Figure S13a,b). In contrast, the expression and

recruitment of integrin  $\beta 1$  were found to have been significantly restrained in the “dropping” group (moving the aggregates downward) compared to the “stationary” group of “low” ligand dispersity. Corresponding computations of the fluorescence signal intensities of integrin  $\beta 1$  and the density of integrin  $\beta 1$ -labeling AuNPs corroborated the trend observed in the fluorescence imaging and nanoscale immunogold labeling (Figure 5b and Supplementary Figure S13b). The bright-field images showed that distant manipulation of “dropping” the aggregates in “low” ligand dispersity prevented the recruitment of macrophages underneath the aggregate compared to the “stationary” group as the nanospace between the aggregate and substrate becomes lower (Supplementary Figure S14). The immunofluorescent staining of other adhesion complexes (paxillin and actin) and corresponding quantifications showed similar results (Figure 5c). The expression of paxillin and actin with elongated macrophage morphology was elevated in the “lifting” group compared to the “stationary” group of “high” ligand dispersity. In contrast, the expression of paxillin and actin was significantly decreased in the “dropping” group compared to the “stationary” group of “low” ligand dispersity. None of the magnetic nanoparticle aggregates were shown to be internalized into adherent macrophages (Supplementary Movie S1). Also, the magnetic nanoparticle aggregates exhibited negligible rupture under a magnetic field (Supplementary Movie S2). These results collectively confirm the high stability of our material system.

We concluded that with the two distinct groups of “high” and “low” accessible ligand dispersity, the nanospace that was increased or reduced by the “lifting” or “dropping” of magnetic aggregates, respectively, is laterally different due to their significantly different sizes (200 nm vs 700 nm) despite similar vertical displacement estimated due to the use of identical lengths in the bendy polymer linker. The area blocked by the lower sides of the 200 nm aggregates with “high” accessible ligand dispersity was significantly smaller than that of the 700 nm aggregates with “low” accessible ligand dispersity. In the “stationary” condition, integrin receptors (10 nm) in macrophages can be more readily recruited to the accessible ligands under each 700 nm aggregate than those under each 200 nm aggregate. This significant difference could have led to the highly facilitated receptor–ligand binding via “low” accessible ligand dispersity albeit with lower density of 700 nm aggregates compared to the “high” accessible ligand dispersity with higher density of 200 nm aggregates. Furthermore, the large accessible liganded area with 700 nm aggregates could be more readily reduced by “dropping” them, which effectively suppressed integrin recruitment and adhesion assemblies in macrophages. Conversely, the small accessible liganded area with 200 nm aggregates could be readily enlarged by “lifting” them, which effectively augmented integrin recruitment and adhesion assemblies in macrophages. Since the size of integrins lies in 10 nm, the recruitment of integrin receptors to the accessible ligands after moving the spherical 200 or 700 nm aggregates can be readily and optimally manipulated. Negative control experiments using distant manipulation without ligand coating on the AuNPs or RAD (scrambled RGD)-coated AuNPs exhibited minimal adhesion of macrophages in all groups, thereby confirming the specificity of the distant manipulation of ligand accessibility for regulating macrophages (Supplementary Figures S15a,b and S16a,b).

Additionally, we analyzed macrophage adhesion with high accessible ligand dispersity (the “stationary” and “lifting”

groups) and low accessible ligand dispersity (the “stationary” and “dropping” groups) after 36 h of culturing. We found that the effect of distant manipulation of magnetic aggregates on the regulation of macrophage adhesion was not saturated; rather, it had higher effect after 36 h than 24 h of culturing (Supplementary Figure S17a,b). Strikingly, negative control experiments using distant manipulation without the ligand coating on the AuNPs or RAD (scrambled RGD)-coated AuNPs have exhibited significant differences on the regulation of macrophage adhesion after 36 h of culturing, which was not observed after 24 h (Supplementary Figures S18a,b and S19a,b). This suggests that the accessibility of nonspecific binding sites under aggregates was also controlled by distant manipulation to regulate macrophage adhesion. Since the efficiency of nonspecific binding is highly lower than that of the RGD-specific binding, it may have taken a longer time to regulate macrophage adhesion. Therefore, we used “24 h” as the culturing period in our system to regulate macrophage adhesion by controlling receptor–ligand binding via manipulation of the accessibility of integrin-specific RGD binding sites.

**Distant Manipulation of Ligand Accessibility Modulation Regulates Macrophage Adhesion-Dependent Polarization.** It has been shown in many studies that macrophages exhibiting pronounced binding of integrin receptors to the ligands trigger the formation of F-actin and adhesion complexes (e.g., paxillin) in cytoskeletons with elongated and spread morphology and acquire pro-healing M2 polarization involving rho-associated protein kinase (ROCK) signaling.<sup>72–75</sup> Conversely, macrophages poorly adhering to ligand-presenting surfaces polarize into inflammatory M1 phenotype. Therefore, the effect of distant manipulation of the aggregates to modulate the ligand accessibility on the adhesion complex assembly dependent macrophage polarization was investigated after 36 h of culturing in M1 or M2 induction medium. In “high” ligand dispersity, the expression of CD68 implying the involvement of inflammation was found to be significantly suppressed in the “lifting” group compared to the “stationary” group as evidenced by the immunofluorescently stained images (Supplementary Figure S20a). Concomitantly, in “high” ligand dispersity, the expression of Arg-1 signifying anti-inflammation was found to be significantly augmented in the “lifting” group compared to the “stationary” group. On the other hand, in “low” ligand dispersity, the expression of CD68 was found to be significantly elevated in the “dropping” group compared to the “stationary” group (Supplementary Figure S20a). Simultaneously, in “low” ligand dispersity, the expression of Arg-1 was found to be significantly hindered in the “dropping” group compared to the “stationary” group.

Next, we evaluated the effect of distant manipulation of the magnetic aggregates to modulate the ligand accessibility on M1 or M2 macrophage polarization via Western blotting-based protein quantifications. With “high” ligand dispersity, the expression of iNOS (M1 polarization-specific marker) was significantly suppressed in the “lifting” group compared to the “stationary” group, whereas the expression of Arg-1 (M2 polarization-specific marker) was significantly promoted in the “lifting” group compared to the “stationary” group (Supplementary Figure S20b,c). In contrast, with “low” ligand dispersity in the “dropping” group compared to the “stationary” group, the expression of iNOS was significantly stimulated, whereas the expression of Arg-1 was significantly

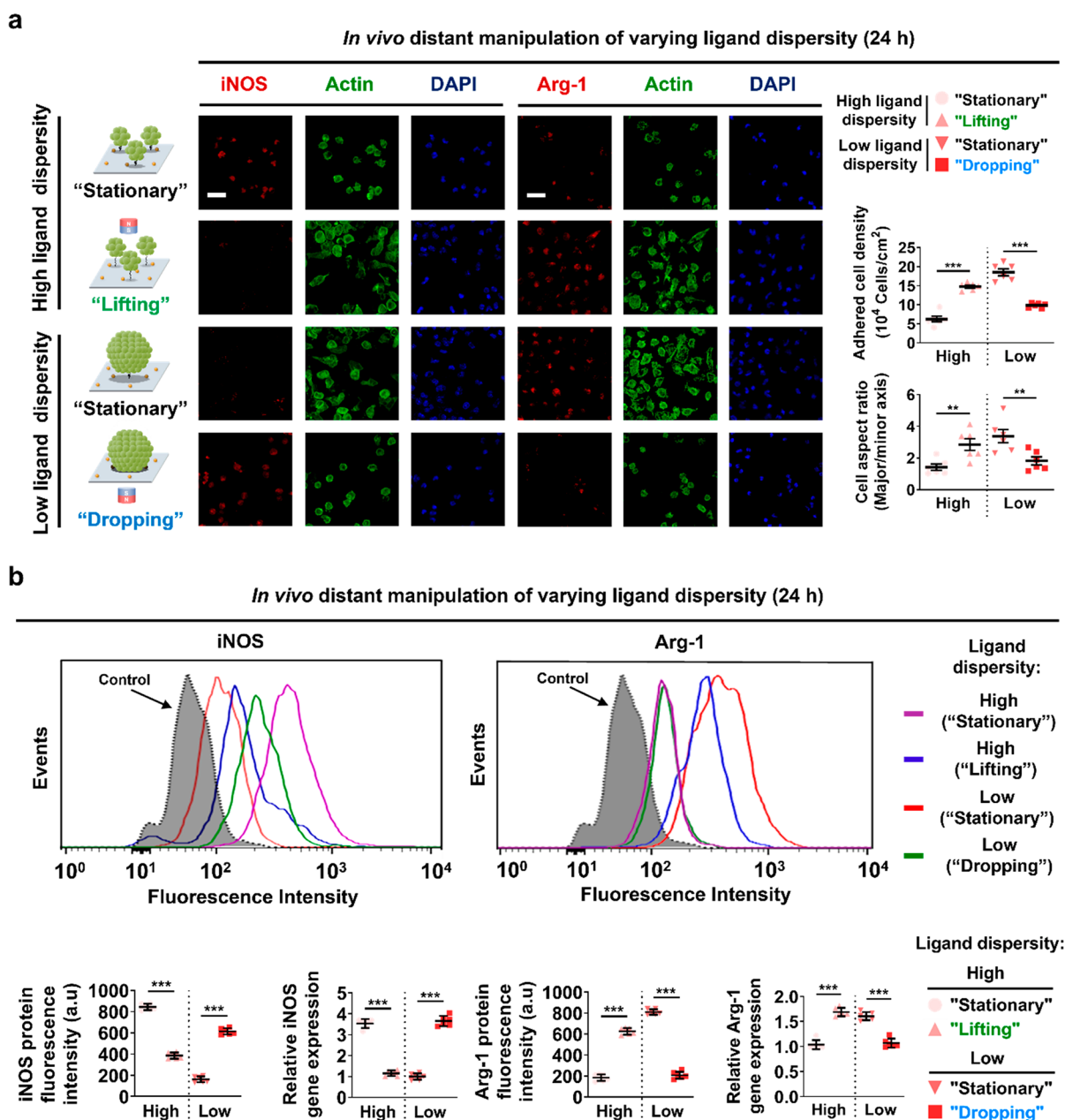


**Figure 6.** Both low accessible ligand dispersy and distant manipulation of increasing ligand accessibility stimulate integrin ligation-mediated adhesion and anti-inflammatory polarization of host macrophages. (a) Immunofluorescently stained images of M1 marker (iNOS) or M2 marker (Arg-1) costained along with F-actin and DAPI (nuclei) in the recruited adherent macrophages after 24 h of subcutaneous implantation into mice in the presence of high accessible ligand dispersy (the “stationary” group without a magnet and the “lifting” group with a magnet attached to the backs of the mice) as well as low accessible ligand dispersy (the “stationary” group without a magnet and the “dropping” group with a magnet attached to the abdomens of the mice). The scale bars denote 20  $\mu\text{m}$ . Corresponding computations of the adherent macrophage density and aspect ratio are also shown, which were statistically compared separately in each high or low accessible ligand dispersy group using a two-tailed Student’s *t* test. Asterisks were assigned to *p* values with statistically significant significances (\*\**p* < 0.01; \*\*\**p* < 0.001). (b) Flow cytometry histograms of iNOS and Arg-1 and corresponding computations of their protein fluorescence intensities and relative gene expression levels, which were subjected to identical statistical analysis to compare each high or low accessible ligand dispersy group. Data are shown as the mean  $\pm$  standard error (*n* = 6).

inhibited. These trends consistently reveal that “low” ligand dispersy effectively intensifies the binding of integrin receptors to the accessible ligands to mediate pro-healing M2 macrophage polarization compared to the “high” ligand dispersy. These findings also verify that with “high” ligand dispersy, the effective direction of “lifting” considerably intensifies integrin-ligand binding to mediate macrophage M2 polarization and suppress M1 polarization. With “low” ligand dispersy, the effective “dropping” direction substantially

suppresses integrin-ligand binding and macrophage M2 polarization.

We next pondered which molecular machinery is involved in this efficient regulation of the adhesion-dependent macrophage polarization. In this investigation, we included both static groups of “low” and “high” ligand dispersy in the “stationary” condition. Since “high” ligand dispersy under distant manipulation of “lifting” the aggregates (to increase the ligand accessibility) significantly facilitated the adhesion-mediated M2

polarization of macrophages, this group was included as the formation of molecular machinery could have been involved. Contrastively, since “low” ligand dispersity under distant manipulation of “dropping” the aggregates (to decrease the ligand accessibility) significantly suppressed the adhesion assembly in macrophages, we excluded this group. Both groups of “low” ligand dispersity in the “stationary” condition and “high” ligand dispersity under distant manipulation of “lifting” the aggregates efficiently promoted ROCK2 expression and the adhesion-assisted M2 polarization of macrophages compared with “high” ligand dispersity in the “stationary” condition (Supplementary Figure S21). This relationship between the adhesion complex assembly and consequential polarization was examined using inhibitors specific for myosin II (blebbistatin), actin polymerization (cytochalasin D), and ROCK (Y27632). With “high” ligand dispersity in the “stationary” condition, CD68 expression (implying the involvement of inflammation) was promoted with and without inhibitors (Supplementary Figure S22a,b). Contrastively, all of the inhibitors were found to promote CD68 expression in the “low” ligand dispersity under the “stationary” condition and the “high” ligand dispersity under the “lifting” condition, which was suppressed without inhibitors. With “high” ligand dispersity in the “stationary” condition, a low degree of Arg-1 expression was observed with and without inhibitors (Supplementary Figure S23a,b). Furthermore, all of the inhibitors were found to hinder Arg-1 expression with “low” ligand dispersity under the “stationary” condition and “high” ligand dispersity under the “lifting” condition, which was highly expressed in the absence of inhibitors. These findings collectively prove that myosin II, actin polymerization, and ROCK are involved in the molecular mechanism with “low” accessible ligand dispersity and distant manipulation of increasing the ligand accessibility that augments the binding of integrin receptors to the accessible ligands to stimulate anti-inflammatory M2 polarization of macrophages while restraining inflammatory M1 polarization.

**Remotely Controlling the Ligand Accessibility for Host Macrophage Regulation.** When tissues are damaged, the recruitment of macrophages and the regulation of the inflammatory and tissue-regenerative responses are modulated.<sup>3,76,77</sup> Controlling the early host response dominated by macrophages (which trigger acute inflammation and tissue healing in response to the implanted biomaterials) can proportionally lead to regulation of the long-term response, including tissue healing and fibrosis.<sup>33,43,78</sup> To this end, the remote control effect of modulating ligand accessibility to dynamically vary the ligand dispersity on regulating recruited host macrophages in vivo by utilizing a highly tissue-penetrative magnetic field was examined. The materials presenting magnetic aggregates over liganded AuNPs were subcutaneously implanted into mice (Supplementary Figure S24). While no magnet was attached to the mice in the “stationary” condition, a magnet was attached at the backs or abdomens of mice to direct “lifting” (for increasing the ligand accessibility) or “dropping” (for decreasing the ligand accessibility) of the magnetic aggregates, respectively. It has been previously reported Fe<sub>3</sub>O<sub>4</sub> nanoparticle-based implanted materials are not toxic to humans,<sup>79</sup> and that a strong magnetic field is harmless to humans.<sup>80</sup> These reports indicate that our implanted materials involving magnetic nanoparticle aggregates and their distant manipulation under the magnetic field could be used safely in humans. The implanted materials were

collected at 24 h postimplantation to verify their stability after being subjected to distant manipulation of the magnetic aggregates over ligand-coated AuNPs on the materials by examining their in vivo degradation. We demonstrated that the ligand-coated AuNPs and the aggregates with or without magnetic manipulation were all retained in the materials without degradation after implantation via SEM imaging and corresponding computations (Supplementary Figure S25a,b).

The recruited host macrophages onto the materials were analyzed by immunofluorescent staining imaging, flow cytometry quantification, and quantitative polymerase chain reaction (qPCR). Immunofluorescent costaining of inflammatory M1 polarization-specific marker (iNOS) and M2 polarization-specific marker (Arg-1), along with F-actin and DAPI (nuclear staining) was performed to examine F-actin assembled as a result of receptor–ligand binding in the recruited host macrophages. With “high” ligand dispersity, in the “lifting” group, the adhesion complex (F-actin assembly) and Arg-1 were significantly intensified while iNOS expression was substantially suppressed compared to the “stationary” group (Figure 6a and Supplementary Figure S26). Conversely, with “low” ligand dispersity, in the “dropping” group, the adhesion complex and Arg-1 expression were significantly suppressed while iNOS expression was considerably stimulated compared to the “stationary” group. Indeed, flow cytometry histograms with quantifications and qPCR-based relative gene expression levels of host cells consistently corroborated these trends (Figure 6b). Taken together, flow cytometry and qPCR results consistently supported the observations that the “dropping” condition in low ligand dispersity switched pronounced Arg-1 expression (observed in the “stationary” condition) to marked iNOS expression.

Furthermore, not only the host macrophages but also the host neutrophils (NIMP-R14-positive), predominant immune cells appearing in the early host response that proportionally regulate the long-term immune responses, were recruited onto the implanted materials (Supplementary Figure S27a,b). The outcomes of this study consistently prove that with “high” ligand dispersity, “lifting” the magnetic aggregates in vivo remarkably augments host macrophage adhesion and pro-healing polarization plausibly as a result of facilitated binding of integrin receptors to the ligands. Conversely, with “low” ligand dispersity, “dropping” the magnetic aggregates in vivo strikingly suppresses host macrophage adhesion but intensifies M1 polarization. This distant manipulation is apparently different from previous in vivo studies of modulating the entire ligand accessibility on the material surface by changing heterodimer conformations (i.e., devoid of partial control of ligand accessibility)<sup>58</sup> or by tissue-absorptive UV light illumination (devoid of partial control of ligand accessibility and reversibility).<sup>43</sup> Our multimodal manipulation of the partial ligand accessibility using the magnetic aggregates enables host macrophage regulation and associated host responses.

## CONCLUSIONS

In summary, we fabricated materials by harnessing magnetic nanoparticle aggregates of adjustable sizes (200, 500, and 700 nm) and conjugated them to the material surface presenting ligand-bearing AuNPs via bendy polymer linker. Specifically, we increased or decreased the concentration of cationic capping surfactant (DTAB) during magnetic nanoparticle aggregation to adjust the aggregates into smaller or larger sizes,

respectively. Lowering the accessible ligand dispersity by increasing the aggregate size as a novel parameter (without varying the accessible ligand density) independently facilitated the binding of integrin receptors to the accessible ligands in the assembly of adhesion complexes in macrophages and pro-healing polarization both in vitro and in vivo. With “high” ligand dispersity, distant manipulation of lifting the aggregates relatively increases the ligand accessibility via the linker straightening, which stimulates integrin recruitment to the accessible ligands for macrophage adhesion both in vitro and in vivo, involving the molecular machinery of myosin II, F-actin, and ROCK. With “low” ligand dispersity, distant control of dropping aggregates relatively decreases the ligand accessibility via linker bending, which repels integrins away from the aggregates and suppresses macrophage adhesion. This is the first demonstration of the multimodal and reversible manipulation of ligand accessibility modulation on material surfaces for macrophage regulation.

## ■ ASSOCIATED CONTENT

### SI Supporting Information

The Supporting Information is available free of charge at <https://pubs.acs.org/doi/10.1021/jacs.1c08861>.

Supplementary Movie S1: The internalization of magnetic nanoparticle aggregates into macrophages is negligible (MP4)

Supplementary Movie S2: Negligible physical rupture of magnetic nanoparticle aggregates under a magnetic field (MP4)

Experimental Section: Characterization of magnetic nanoparticle aggregates composed of iron oxide nanoparticle ensemble (via SAD pattern, zeta potential, FTIR, TEM, DLS, VSM, AFM, and SEM); distant manipulation of the accessible ligand dispersity on integrin  $\beta 1$  expression, macrophage adhesion and polarization involving myosin II, actin polymerization, and ROCK; substrate stability in vivo; host macrophage and neutrophil adhesion (confocal immunofluorescence imaging, Western blotting, and SEM) (PDF)

## ■ AUTHOR INFORMATION

### Corresponding Authors

**Dokyoon Kim** – Center for Nanoparticle Research, Institute for Basic Science (IBS), Seoul 08826, Republic of Korea; Department of Bionano Engineering and Bionanotechnology, Hanyang University, Ansan 15588, Republic of Korea; Email: [kimdk@hanyang.ac.kr](mailto:kimdk@hanyang.ac.kr)

**Heemin Kang** – Department of Materials Science and Engineering and Department of Biomicrosystem Technology, Korea University, Seoul 02841, Republic of Korea; [orcid.org/0000-0003-2694-9882](https://orcid.org/0000-0003-2694-9882); Email: [heeminkang@korea.ac.kr](mailto:heeminkang@korea.ac.kr)

### Authors

**Yuri Kim** – Department of Materials Science and Engineering, Korea University, Seoul 02841, Republic of Korea

**Hee Joon Jung** – Department of Materials Science and Engineering, International Institute for Nanotechnology, and NUANCE Center, Northwestern University, Evanston, Illinois 60208, United States; [orcid.org/0000-0001-7963-0897](https://orcid.org/0000-0001-7963-0897)

**Yunjung Lee** – Center for Nanoparticle Research, Institute for Basic Science (IBS), Seoul 08826, Republic of Korea; School of Chemical and Biological Engineering, Seoul National University, Seoul 08826, Republic of Korea

**Sagang Koo** – Center for Nanoparticle Research, Institute for Basic Science (IBS), Seoul 08826, Republic of Korea; School of Chemical and Biological Engineering, Seoul National University, Seoul 08826, Republic of Korea; [orcid.org/0000-0001-8154-7881](https://orcid.org/0000-0001-8154-7881)

**Ramar Thangam** – Department of Materials Science and Engineering, Korea University, Seoul 02841, Republic of Korea; [orcid.org/0000-0002-6209-7149](https://orcid.org/0000-0002-6209-7149)

**Woo Young Jang** – Department of Orthopedic Surgery, Korea University Anam Hospital, Seoul 02841, Republic of Korea

**Seong Yeol Kim** – Department of Materials Science and Engineering, Korea University, Seoul 02841, Republic of Korea

**Sangwoo Park** – Department of Materials Science and Engineering, Korea University, Seoul 02841, Republic of Korea

**Sungkyu Lee** – Department of Materials Science and Engineering, Korea University, Seoul 02841, Republic of Korea

**Gunhyu Bae** – Department of Materials Science and Engineering, Korea University, Seoul 02841, Republic of Korea

**Kapil Dev Patel** – Department of Materials Science and Engineering, Korea University, Seoul 02841, Republic of Korea

**Qiang Wei** – College of Polymer Science and Engineering, State Key Laboratory of Polymer Materials and Engineering, Sichuan University, Chengdu 610065, China; [orcid.org/0000-0001-5194-8262](https://orcid.org/0000-0001-5194-8262)

**Ki-Bum Lee** – Department of Chemistry and Chemical Biology, Rutgers University, Piscataway, New Jersey 08854, United States; [orcid.org/0000-0002-8164-0047](https://orcid.org/0000-0002-8164-0047)

**Ramasamy Paulmurugan** – Department of Radiology, Molecular Imaging Program at Stanford, Stanford University School of Medicine and Department of Radiology, Canary Center at Stanford for Cancer Early Detection, Stanford University School of Medicine, Stanford University, Palo Alto, California 94304, United States; [orcid.org/0000-0001-7155-4738](https://orcid.org/0000-0001-7155-4738)

**Woong Kyo Jeong** – Department of Orthopedic Surgery, Korea University Anam Hospital, Seoul 02841, Republic of Korea

**Taeghwan Hyeon** – Center for Nanoparticle Research, Institute for Basic Science (IBS), Seoul 08826, Republic of Korea; School of Chemical and Biological Engineering, Seoul National University, Seoul 08826, Republic of Korea; [orcid.org/0000-0001-5959-6257](https://orcid.org/0000-0001-5959-6257)

Complete contact information is available at: <https://pubs.acs.org/10.1021/jacs.1c08861>

### Author Contributions

<sup>†</sup>Y.K. and H.J.J. contributed equally to this work.

### Notes

The authors declare no competing financial interest.

## ■ ACKNOWLEDGMENTS

This work was supported by the National Research Foundation of Korea (NRF) grant funded by the Korea

government (MSIT) (No. 2020R1C1C1011038 and 2022R1A2C1003527). This work was also supported by a Korea University Grant. HAADF-STEM imaging was conducted with the support of the Seoul center in Korea Basic Science Institute (KBSI). This work made use of the EPIC facility of Northwestern University's NUANCE Center, which has received support from the Soft and Hybrid Nanotechnology Experimental (SHyNE) Resource (NSF ECCS-1542205), the MRSEC IRG2 program (NSF DMR-1720139) at the Materials Research Center, the International Institute for Nanotechnology (IIN), the Keck Foundation, and the State of Illinois, through the IIN.

## REFERENCES

- (1) Yeste, J.; Illa, X.; Alvarez, M.; Villa, R. Engineering and monitoring cellular barrier models. *J. Biol. Eng.* **2018**, *12*, 1–19.
- (2) Louis, N. A.; Lin, P. W. The intestinal immune barrier. *Neoreviews* **2009**, *10*, e180–e190.
- (3) Keaney, J.; Campbell, M. The dynamic blood-brain barrier. *FEBS J.* **2015**, *282*, 4067–4079.
- (4) Lin, X.; Wang, Q.; Gu, C.; Li, M.; Chen, K.; Chen, P.; Tang, Z.; Liu, X.; Pan, H.; Liu, Z.; et al. Smart Nanosacrificial Layer on the Bone Surface Prevents Osteoporosis through Acid–Base Neutralization Regulated Biocascade Effects. *J. Am. Chem. Soc.* **2020**, *142*, 17543–17556.
- (5) Yao, C.; Tang, H.; Wu, W.; Tang, J.; Guo, W.; Luo, D.; Yang, D. Double rolling circle amplification generates physically cross-linked DNA network for stem cell fishing. *J. Am. Chem. Soc.* **2020**, *142*, 3422–3429.
- (6) Suresh, B. M.; Li, W.; Zhang, P.; Wang, K. W.; Yildirim, I.; Parker, C. G.; Disney, M. D. A general fragment-based approach to identify and optimize bioactive ligands targeting RNA. *Proc. Natl. Acad. Sci. U. S. A.* **2020**, *117*, 33197–33203.
- (7) Wang, H.; Mooney, D. J. Biomaterial-assisted targeted modulation of immune cells in cancer treatment. *Nat. Mater.* **2018**, *17*, 761–772.
- (8) Kim, K. S.; Lee, J. Y.; Han, J.; Hwang, H. S.; Lee, J.; Na, K. Local Immune-Triggered Surface-Modified Stem Cells for Solid Tumor Immunotherapy. *Adv. Funct. Mater.* **2019**, *29*, 1900773.
- (9) Lee, J. S.; Roh, Y. H.; Choi, Y. S.; Jin, Y.; Jeon, E. J.; Bong, K. W.; Cho, S. W. Tissue Beads: Tissue-Specific Extracellular Matrix Microbeads to Potentiate Reprogrammed Cell-Based Therapy. *Adv. Funct. Mater.* **2019**, *29*, 1807803.
- (10) Sadtler, K.; Singh, A.; Wolf, M. T.; Wang, X. K.; Pardoll, D. M.; Elisseeff, J. H. Design, clinical translation and immunological response of biomaterials in regenerative medicine. *Nat. Rev. Mater.* **2016**, *1*, 1–17.
- (11) Sadtler, K.; Estrellas, K.; Allen, B. W.; Wolf, M. T.; Fan, H. N.; Tam, A. J.; Patel, C. H.; Lubber, B. S.; Wang, H.; Wagner, K. R.; Powell, J. D.; Housseau, F.; Pardoll, D. M.; Elisseeff, J. H. Developing a pro-regenerative biomaterial scaffold microenvironment requires T helper 2 cells. *Science* **2016**, *352*, 366–370.
- (12) Lei, Q.; Guo, J.; Kong, F.; Cao, J.; Wang, L.; Zhu, W.; Brinker, C. J. Bioinspired Cell Silicification: From Extracellular to Intracellular. *J. Am. Chem. Soc.* **2021**, *143*, 6305–6322.
- (13) Qian, R.-C.; Zhou, Z.-R.; Guo, W.; Wu, Y.; Yang, Z.; Lu, Y. Cell Surface Engineering Using DNazymes: Metal Ion Mediated Control of Cell–Cell Interactions. *J. Am. Chem. Soc.* **2021**, *143*, 5737–5744.
- (14) Levine, Z. G.; Potter, S. C.; Joiner, C. M.; Fei, G. Q.; Nabet, B.; Sonnett, M.; Zachara, N. E.; Gray, N. S.; Paulo, J. A.; Walker, S. Mammalian cell proliferation requires noncatalytic functions of O-GlcNAc transferase. *Proc. Natl. Acad. Sci. U. S. A.* **2021**, *118*, e2016778118.
- (15) Li, J. H.; Jiang, X. Q.; Li, H. J.; Gelinsky, M.; Gu, Z. Tailoring Materials for Modulation of Macrophage Fate. *Adv. Mater.* **2021**, *33*, 2004172.
- (16) Chen, H.; Shi, T.; Wang, Y.; Liu, Z.; Liu, F.; Zhang, H.; Wang, X.; Miao, Z.; Liu, B.; Wan, M.; et al. Deep Penetration of Nanolevel Drugs and Micrometer-Level T Cells Promoted by Nanomotors for Cancer Immunotherapy. *J. Am. Chem. Soc.* **2021**, *143*, 12025–12037.
- (17) Choo, P.; Liu, T.; Odom, T. W. Nanoparticle shape determines dynamics of targeting nanoconstructs on cell membranes. *J. Am. Chem. Soc.* **2021**, *143*, 4550–4555.
- (18) Lacroix, A.; Sleiman, H. F. DNA Nanostructures: Current Challenges and Opportunities for Cellular Delivery. *ACS Nano* **2021**, *15*, 3631–3645.
- (19) Song, Y.; Elsbahy, M.; Collins, C. A.; Khan, S.; Li, R.; Hreh, T. N.; Shen, Y.; Lin, Y.-N.; Letteri, R. A.; Su, L.; et al. Morphologic Design of Silver-Bearing Sugar-Based Polymer Nanoparticles for Uroepithelial Cell Binding and Antimicrobial Delivery. *Nano Lett.* **2021**, *21*, 4990–4998.
- (20) Wu, Y.; Alam, M. N. A.; Balasubramanian, P.; Ermakova, A.; Fischer, S.; Barth, H.; Wagner, M.; Raabe, M.; Jelezko, F.; Weil, T. Nanodiamond Theranostic for Light-Controlled Intracellular Heating and Nanoscale Temperature Sensing. *Nano Lett.* **2021**, *21*, 3780–3788.
- (21) Huang, J.; Grater, S. V.; Corbellini, F.; Rinck, S.; Bock, E.; Kemkemer, R.; Kessler, H.; Ding, J.; Spatz, J. P. Impact of Order and Disorder in RGD Nanopatterns on Cell Adhesion. *Nano Lett.* **2009**, *9*, 1111–1116.
- (22) Chen, C. S.; Mrksich, M.; Huang, S.; Whitesides, G. M.; Ingber, D. E. Geometric control of cell life and death. *Science* **1997**, *276*, 1425–1428.
- (23) Deeg, J. A.; Louban, I.; Aydin, D.; Selhuber-Unkel, C.; Kessler, H.; Spatz, J. P. Impact of Local versus Global Ligand Density on Cellular Adhesion. *Nano Lett.* **2011**, *11*, 1469–1476.
- (24) Staufer, O.; Antona, S.; Zhang, D.; Csatari, J.; Schroter, M.; Janiesch, J. W.; Fabritz, S.; Berger, I.; Platzman, I.; Spatz, J. P. Microfluidic production and characterization of biofunctionalized giant unilamellar vesicles for targeted intracellular cargo delivery. *Biomaterials* **2021**, *264*, 120203.
- (25) Wang, X.; Li, S. Y.; Yan, C.; Liu, P.; Ding, J. D. Fabrication of RGD Micro/Nanopattern and Corresponding Study of Stem Cell Differentiation. *Nano Lett.* **2015**, *15*, 1457–1467.
- (26) Ye, K.; Wang, X.; Cao, L. P.; Li, S. Y.; Li, Z. H.; Yu, L.; Ding, J. D. Matrix Stiffness and Nanoscale Spatial Organization of Cell-Adhesive Ligands Direct Stem Cell Fate. *Nano Lett.* **2015**, *15*, 4720–4729.
- (27) Koo, L. Y.; Irvine, D. J.; Mayes, A. M.; Lauffenburger, D. A.; Griffith, L. G. Co-regulation of cell adhesion by nanoscale RGD organization and mechanical stimulus. *J. Cell Sci.* **2002**, *115*, 1423–1433.
- (28) Deng, J.; Zhao, C. S.; Spatz, J. P.; Wei, Q. Nanopatterned Adhesive, Stretchable Hydrogel to Control Ligand Spacing and Regulate Cell Spreading and Migration. *ACS Nano* **2017**, *11*, 8282–8291.
- (29) Glazier, R.; Brockman, J. M.; Bartle, E.; Mattheyses, A. L.; Destaing, O.; Salaita, K. DNA mechanotechnology reveals that integrin receptors apply pN forces in podosomes on fluid substrates. *Nat. Commun.* **2019**, *10*, 1–13.
- (30) Zaveri, T. D.; Lewis, J. S.; Dolgova, N. V.; Clare-Salzler, M. J.; Keselowsky, B. G. Integrin-directed modulation of macrophage responses to biomaterials. *Biomaterials* **2014**, *35*, 3504–3515.
- (31) Wu, D.; Li, J.; Xu, S.; Xie, Q.; Pan, Y.; Liu, X.; Ma, R.; Zheng, H.; Gao, M.; Wang, W.; et al. Engineering Fe–N doped graphene to mimic biological functions of NADPH oxidase in cells. *J. Am. Chem. Soc.* **2020**, *142*, 19602–19610.
- (32) Ni, K.; Luo, T.; Culbert, A.; Kaufmann, M.; Jiang, X.; Lin, W. Nanoscale metal–organic framework co-delivers TLR-7 agonists and anti-CD47 antibodies to modulate macrophages and orchestrate cancer immunotherapy. *J. Am. Chem. Soc.* **2020**, *142*, 12579–12584.
- (33) Han, J.; Kim, Y. S.; Lim, M. Y.; Kim, H. Y.; Kong, S.; Kang, M.; Choo, Y. W.; Jun, J. H.; Ryu, S.; Jeong, H. Y.; Park, J.; Jeong, G. J.; Lee, J. C.; Eom, G. H.; Ahn, Y.; Kim, B. S. Dual Roles of Graphene Oxide To Attenuate Inflammation and Elicit Timely Polarization of

Macrophage Phenotypes for Cardiac Repair. *ACS Nano* **2018**, *12*, 1959–1977.

(34) Kim, J.; Kim, H. Y.; Song, S. Y.; Go, S. H.; Sohn, H. S.; Baik, S.; Soh, M.; Kim, K.; Kim, D.; Kim, H. C.; Lee, N.; Kim, B. S.; Hyeon, T. Synergistic Oxygen Generation and Reactive Oxygen Species Scavenging by Manganese Ferrite/Ceria Co-decorated Nanoparticles for Rheumatoid Arthritis Treatment. *ACS Nano* **2019**, *13*, 3206–3217.

(35) Taha, M. S.; Cresswell, G. M.; Park, J.; Lee, W.; Ratliff, T. L.; Yeo, Y. Sustained Delivery of Carfilzomib by Tannic Acid-Based Nanocapsules Helps Develop Antitumor Immunity. *Nano Lett.* **2019**, *19*, 8333–8341.

(36) Wang, H. R.; Han, X.; Dong, Z. L.; Xu, J.; Wang, J.; Liu, Z. Hyaluronidase with pH-responsive Dextran Modification as an Adjuvant Nanomedicine for Enhanced Photodynamic-Immunotherapy of Cancer. *Adv. Funct. Mater.* **2019**, *29*, 1902440.

(37) Gomes, B. S.; Simoes, B.; Mendes, P. M. The increasing dynamic, functional complexity of bio-interface materials. *Nat. Rev. Chem.* **2018**, *2*, 1–15.

(38) Kim, Y.; Choi, H.; Shin, J. E.; Bae, G.; Thangam, R.; Kang, H. Remote active control of nanoengineered materials for dynamic nanobiomedical engineering. *View* **2020**, *1*, 20200029.

(39) Parasar, B.; Chang, P. V. Engineered Th17 Cell Differentiation Using a Photoactivatable Immune Modulator. *J. Am. Chem. Soc.* **2020**, *142*, 18103–18108.

(40) Weyandt, E.; Ter Huurne, G. M.; Vantomme, G.; Markvoort, A. J.; Palmans, A. R.; Meijer, E. Photodynamic control of the chain length in supramolecular polymers: switching an intercalator into a chain capper. *J. Am. Chem. Soc.* **2020**, *142*, 6295–6303.

(41) Sarott, R. C.; Viray, A. E.; Pfaff, P.; Sadybekov, A.; Rajic, G.; Katritch, V.; Carreira, E. M.; Frank, J. A. Optical Control of Cannabinoid Receptor 2-Mediated Ca<sup>2+</sup> Release Enabled by Synthesis of Photoswitchable Probes. *J. Am. Chem. Soc.* **2021**, *143*, 736–743.

(42) Xie, Y.; Arno, M. C.; Husband, J. T.; Torrent-Sucarrat, M.; O'Reilly, R. K. Manipulating the fluorescence lifetime at the sub-cellular scale via photo-switchable barcoding. *Nat. Commun.* **2020**, *11*, 1–9.

(43) Lee, T. T.; Garcia, J. R.; Paez, J. I.; Singh, A.; Phelps, E. A.; Weis, S.; Shafiq, Z.; Shekaran, A.; del Campo, A.; Garcia, A. J. Light-triggered in vivo activation of adhesive peptides regulates cell adhesion, inflammation and vascularization of biomaterials. *Nat. Mater.* **2015**, *14*, 352–360.

(44) Li, W.; Yan, Z.; Ren, J.; Qu, X. Manipulating cell fate: dynamic control of cell behaviors on functional platforms. *Chem. Soc. Rev.* **2018**, *47*, 8639–8684.

(45) Li, W.; Wang, J. S.; Ren, J. S.; Qu, X. G. Near-Infrared Upconversion Controls Photocaged Cell Adhesion. *J. Am. Chem. Soc.* **2014**, *136*, 2248–2251.

(46) Liu, D. B.; Xie, Y. Y.; Shao, H. W.; Jiang, X. Y. Using Azobenzene-Embedded Self-Assembled Monolayers To Photochemically Control Cell Adhesion Reversibly. *Angew. Chem., Int. Ed.* **2009**, *48*, 4406–4408.

(47) Kadem, L. F.; Holz, M.; Suana, K. G.; Li, Q.; Lamprecht, C.; Herges, R.; Selhuber-Unkel, C. Rapid Reversible Photoswitching of Integrin-Mediated Adhesion at the Single-Cell Level. *Adv. Mater.* **2016**, *28*, 1799–1802.

(48) Kadem, L. F.; Suana, K. G.; Holz, M.; Wang, W.; Westerhaus, H.; Herges, R.; Selhuber-Unkel, C. High-Frequency Mechanostimulation of Cell Adhesion. *Angew. Chem., Int. Ed.* **2017**, *56*, 225–229.

(49) Kim, J. W.; Seo, D.; Lee, J. U.; Southard, K. M.; Lim, Y.; Kim, D.; Gartner, Z. J.; Jun, Y. W.; Cheon, J. Single-cell mechanogenetics using monovalent magnetoplasmonic nanoparticles. *Nat. Protoc.* **2017**, *12*, 1871–1889.

(50) Kim, J. W.; Jeong, H. K.; Southard, K. M.; Jun, Y. W.; Cheon, J. Magnetic Nanotweezers for Interrogating Biological Processes in Space and Time. *Acc. Chem. Res.* **2018**, *51*, 839–849.

(51) Du, Y.; Yang, C.; Li, F. Y.; Liao, H. W.; Chen, Z.; Lin, P. H.; Wang, N.; Zhou, Y.; Lee, J. Y.; Ding, Q.; Ling, D. S. Core-Shell-

Satellite Nanomeres as Remotely Controlled Self-Fueling Fenton Reagents for Imaging-Guided Triple-Negative Breast Cancer-Specific Therapy. *Small* **2020**, *16*, 2002537.

(52) Pan, J.; Hu, P.; Guo, Y. D.; Hao, J. N.; Ni, D. L.; Xu, Y. Y.; Bao, Q. Q.; Yao, H. L.; Wei, C. Y.; Wu, Q. S.; Shi, J. L. Combined Magnetic Hyperthermia and Immune Therapy for Primary and Metastatic Tumor Treatments. *ACS Nano* **2020**, *14*, 1033–1044.

(53) Pan, J.; Xu, Y.; Wu, Q.; Hu, P.; Shi, J. Mild Magnetic Hyperthermia-Activated Innate Immunity for Liver Cancer Therapy. *J. Am. Chem. Soc.* **2021**, *143*, 8116–8128.

(54) Yu, B.; Choi, B.; Li, W.; Kim, D.-H. Magnetic field boosted ferroptosis-like cell death and responsive MRI using hybrid vesicles for cancer immunotherapy. *Nat. Commun.* **2020**, *11*, 1–9.

(55) Min, S.; Ko, M. J.; Jung, H. J.; Kim, W.; Han, S. B.; Kim, Y.; Bae, G.; Lee, S.; Thangam, R.; Choi, H.; Li, N.; Shin, J. E.; Jeon, Y. S.; Park, H. S.; Kim, Y. J.; Sukumar, U. K.; Song, J. J.; Park, S. K.; Yu, S. H.; Kang, Y. C.; Lee, K. B.; Wei, Q.; Kim, D. H.; Han, S. M.; Paulmurugan, R.; Kim, Y. K.; Kang, H. Remote Control of Time-Regulated Stretching of Ligand-Presenting Nanocoils In Situ Regulates the Cyclic Adhesion and Differentiation of Stem Cells. *Adv. Mater.* **2021**, *33*, 2008353.

(56) Min, S.; Jeon, Y. S.; Jung, H. J.; Khatua, C.; Li, N.; Bae, G.; Choi, H.; Hong, H.; Shin, J. E.; Ko, M. J.; Ko, H. S.; Jun, I.; Fu, H. E.; Kim, S. H.; Thangam, R.; Song, J. J.; Dravid, V. P.; Kim, Y. K.; Kang, H. Independent Tuning of Nano-Ligand Frequency and Sequences Regulates the Adhesion and Differentiation of Stem Cells. *Adv. Mater.* **2020**, *32*, 2004300.

(57) Khatua, C.; Min, S.; Jung, H. J.; Shin, J. E.; Li, N.; Jun, I.; Liu, H. W.; Bae, G.; Choi, H.; Ko, M. J.; Jeon, Y. S.; Kim, Y. J.; Lee, J.; Ko, M.; Shim, G.; Shin, H.; Lee, S.; Chung, S.; Kim, Y. K.; Song, J. J.; Dravid, V. P.; Kang, H. In Situ Magnetic Control of Macroscale Nanoligand Density Regulates the Adhesion and Differentiation of Stem Cells. *Nano Lett.* **2020**, *20*, 4188–4196.

(58) Kang, H.; Jung, H. J.; Wong, D. S. H.; Kim, S. K.; Lin, S. E.; Chan, K. F.; Zhang, L.; Li, G.; Dravid, V. P.; Bian, L. M. Remote Control of Heterodimeric Magnetic Nanoswitch Regulates the Adhesion and Differentiation of Stem Cells. *J. Am. Chem. Soc.* **2018**, *140*, 5909–5913.

(59) Pieszka, M.; Han, S.; Volkmann, C.; Graf, R.; Lieberwirth, I.; Landfester, K.; Ng, D. Y.; Weil, T. Controlled Supramolecular Assembly Inside Living Cells by Sequential Multistaged Chemical Reactions. *J. Am. Chem. Soc.* **2020**, *142*, 15780–15789.

(60) Park, J.; An, K.; Hwang, Y.; Park, J.-G.; Noh, H.-J.; Kim, J.-Y.; Park, J.-H.; Hwang, N.-M.; Hyeon, T. Ultra-large-scale syntheses of monodisperse nanocrystals. *Nat. Mater.* **2004**, *3*, 891–895.

(61) Torruella, P.; Arenal, R.; De La Peña, F.; Saghi, Z.; Yedra, L.; Eljarrat, A.; López-Conesa, L.; Estrader, M.; López-Ortega, A.; Salazar-Alvarez, G.; et al. 3D visualization of the iron oxidation state in FeO/Fe<sub>3</sub>O<sub>4</sub> core-shell nanocubes from electron energy loss tomography. *Nano Lett.* **2016**, *16*, 5068–5073.

(62) Zhang, Q.-L.; Zheng, D.; Dong, X.; Pan, P.; Zeng, S.-M.; Gao, F.; Cheng, S.-X.; Zhang, X.-Z. A Strategy Based on the Enzyme-Catalyzed Polymerization Reaction of Asp-Phe-Tyr Tripeptide for Cancer Immunotherapy. *J. Am. Chem. Soc.* **2021**, *143*, 5127–5140.

(63) Kao, W. J.; Lee, D.; Schense, J. C.; Hubbell, J. A. Fibronectin modulates macrophage adhesion and FBGC formation: the role of RGD, PHSRN, and PRRARV domains. *J. Biomed. Mater. Res., Part A* **2001**, *55*, 79–88.

(64) Trappmann, B.; Gautrot, J. E.; Connelly, J. T.; Strange, D. G.; Li, Y.; Oyen, M. L.; Stuart, M. A. C.; Boehm, H.; Li, B.; Vogel, V.; Spatz, J. P.; Watt, F. M.; Huck, W. T. S. Extracellular-matrix tethering regulates stem-cell fate. *Nat. Mater.* **2012**, *11*, 642–649.

(65) Attwood, S. J.; Cortes, E.; Haining, A. W. M.; Robinson, B.; Li, D. Y.; Gautrot, J.; Hernandez, A. D. Adhesive ligand tether length affects the size and length of focal adhesions and influences cell spreading and attachment. *Sci. Rep.* **2016**, *6*, 1–11.

(66) Xiong, J. P.; Stehle, T.; Zhang, R. G.; Joachimiak, A.; Frech, M.; Goodman, S. L.; Arnaout, M. A. Crystal structure of the extracellular

segment of integrin alpha V beta 3 in complex with an Arg-Gly-Asp ligand. *Science* **2002**, *296*, 151–155.

(67) Zhao, W.; Hanson, L.; Lou, H.-Y.; Akamatsu, M.; Chowdary, P. D.; Santoro, F.; Marks, J. R.; Grassart, A.; Drubin, D. G.; Cui, Y.; et al. Nanoscale manipulation of membrane curvature for probing endocytosis in live cells. *Nat. Nanotechnol.* **2017**, *12*, 750.

(68) Capozza, R.; Caprettini, V.; Gonano, C. A.; Bosca, A.; Moia, F.; Santoro, F.; De Angelis, F. Cell membrane disruption by vertical micro-/nanopillars: role of membrane bending and traction forces. *ACS Appl. Mater. Interfaces* **2018**, *10*, 29107–29114.

(69) Galic, M.; Jeong, S.; Tsai, F.-C.; Joubert, L.-M.; Wu, Y. I.; Hahn, K. M.; Cui, Y.; Meyer, T. External push and internal pull forces recruit curvature-sensing N-BAR domain proteins to the plasma membrane. *Nat. Cell Biol.* **2012**, *14*, 874–881.

(70) Beckwith, K. S.; Ullmann, S.; Vinje, J.; Sikorski, P. Influence of nanopillar arrays on fibroblast motility, adhesion, and migration mechanisms. *Small* **2019**, *15*, 1902514.

(71) Buch-Månson, N.; Bonde, S.; Bolinsson, J.; Berthing, T.; Nygård, J.; Martinez, K. L. Towards a better prediction of cell settling on nanostructure arrays—simple means to complicated ends. *Adv. Funct. Mater.* **2015**, *25*, 3246–3255.

(72) Zandi, S.; Nakao, S.; Chun, K. H.; Fiorina, P.; Sun, D. W.; Arita, R.; Zhao, M.; Kim, E.; Schueller, O.; Campbell, S.; Taher, M.; Melhorn, M. I.; Schering, A.; Gatti, F.; Tezza, S.; Xie, F.; Vergani, A.; Yoshida, S.; Ishikawa, K.; Yamaguchi, M.; Sasaki, F.; Schmidt-Ullrich, R.; Hata, Y.; Enaida, H.; Yuzawa, M.; Yokomizo, T.; Kim, Y. B.; Sweetnam, P.; Ishibashi, T.; Hafezi-Moghadam, A. ROCK-Isoform-Specific Polarization of Macrophages Associated with Age-Related Macular Degeneration. *Cell Rep.* **2015**, *10*, 1173–1186.

(73) Ballotta, V.; Driessen-Mol, A.; Bouten, C. V. C.; Baaijens, F. P. T. Strain-dependent modulation of macrophage polarization within scaffolds. *Biomaterials* **2014**, *35*, 4919–4928.

(74) McWhorter, F. Y.; Davis, C. T.; Liu, W. F. Physical and mechanical regulation of macrophage phenotype and function. *Cell. Mol. Life Sci.* **2015**, *72*, 1303–1316.

(75) McWhorter, F. Y.; Wang, T. T.; Nguyen, P.; Chung, T.; Liu, W. F. Modulation of macrophage phenotype by cell shape. *Proc. Natl. Acad. Sci. U. S. A.* **2013**, *110*, 17253–17258.

(76) Mathur, A. N.; Zirik, B.; Boothby, I. C.; Tan, M.; Cohen, J. N.; Mauro, T. M.; Mehta, P.; Lowe, M. M.; Abbas, A. K.; Ali, N.; Rosenblum, M. D. Treg-Cell Control of a CXCL5-IL-17 Inflammatory Axis Promotes Hair-Follicle-Stem-Cell Differentiation During Skin-Barrier Repair. *Immunity* **2019**, *50*, 655–667.

(77) Pinheiro, M. A. L.; Kooij, G.; Mizze, M. R.; Kamermans, A.; Enzmann, G.; Lyck, R.; Schwaninger, M.; Engelhardt, B.; de Vries, H. E. Immune cell trafficking across the barriers of the central nervous system in multiple sclerosis and stroke. *Biochim. Biophys. Acta, Mol. Basis Dis.* **2016**, *1862*, 461–471.

(78) Veiseh, O.; Doloff, J. C.; Ma, M. L.; Vegas, A. J.; Tam, H. H.; Bader, A. R.; Li, J.; Langan, E.; Wyckoff, J.; Loo, W. S.; Jhunjhunwala, S.; Chiu, A.; Siebert, S.; Tang, K.; Hollister-Lock, J.; Aresta-Dasilva, S.; Bochenek, M.; Mendoza-Elias, J.; Wang, Y.; Qi, M.; Lavin, D. M.; Chen, M.; Dholakia, N.; Thakrar, R.; Lacik, I.; Weir, G. C.; Oberholzer, J.; Greiner, D. L.; Langer, R.; Anderson, D. G. Size- and shape-dependent foreign body immune response to materials implanted in rodents and non-human primates. *Nat. Mater.* **2015**, *14*, 643–U125.

(79) Maier-Hauff, K.; Ulrich, F.; Nestler, D.; Niehoff, H.; Wust, P.; Thiesen, B.; Orawa, H.; Budach, V.; Jordan, A. Efficacy and safety of intratumoral thermotherapy using magnetic iron-oxide nanoparticles combined with external beam radiotherapy on patients with recurrent glioblastoma multiforme. *JNO* **2011**, *103*, 317–324.

(80) Prothmann, M.; von Knobelsdorff-Brenkenhoff, F.; Topper, A.; Dieringer, M. A.; Shahid, E.; Graessl, A.; Rieger, J.; Lysiak, D.; Thalhammer, C.; Huelnhagen, T.; Kellman, P.; Niendorf, T.; Schulz-Menger, J. High Spatial Resolution Cardiovascular Magnetic Resonance at 7.0 T in Patients with Hypertrophic Cardiomyopathy - First Experiences: Lesson Learned from 7.0 T. *PLoS One* **2016**, *11*, e0148066.